Evolution of dispersion along the extruder during the manufacture of polymer-organoclay nanocomposites

J.M. Barbas*, A.V. Machado, J.A. Covas

Institute of Polymers and Composites (IPC) and I3N, University of Minho, Campus of Azurém, 4800-058 Guimarães, Portugal

Keywords:

On-line monitoring
Rheology
Near-infrared spectroscopy
Polymer nanocomposites

Abstract

Although correlations between the final dispersion level of organoclay nanocomposites and melt mixing conditions in a twin screw extruder have been proposed, the actual lengthwise evolution of dispersion in these machines is still not well understood. Despite their practical importance such studies are difficult, due to the possibility of inducing degradation and/or morphology changes during material collection and/or sample preparation. This work uses on-line rheometry and in-line near-infrared spectroscopy (NIR) to monitor the evolution of dispersion of a PP/PP-g-MA/organoclay system along the axis of twin screw extruder. Regardless of the screw profile utilised, dispersion develops quickly in the first part of the machine, and then it levels-off or decreases, even if the final dispersion levels are significant. In order to validate this data, Scanning Transmitted Electron Microscopy (STEM), X-ray diffraction (XRD) and mid-FT-IR analyses are carried out on samples collected from the same locations where the on-line/in-line measurements were performed. The results confirmed the previous measurements. Thermogravimetric analysis (TGA) and Time of Flight-Secondary Ion Mass Spectrometry (TOF-SIMS) on clay, matrix and nanocomposite showed that thermal degradation of the clay surfactant and of the polymer matrix could contribute to the observed dispersion reversal.

Introduction

Mixing a small amount (typically less than 5wt%) of layered clay particles with a thermoplastic polymer matrix to obtain enhanced properties is often performed directly in the melt, due to the effectiveness of the intercalation-exfoliation levels attained (Vaia et al., 1993; Cho and Paul, 2001; Dennis et al., 2001; Pavlidou and Papaspyrides, 2008) and the suitability of this route to

industrial scale production (Cho and Paul, 2001; Dennis et al., 2001). Many authors investigated the effects of the molecular weight of the matrix (Fornes et al., 2001; Kim et al., 2002; Tanoue et al., 2004), the chemical affinity of the polymer-clay interface (Tanoue et al., 2004; Modesti et al., 2005; Xu et al., 2009) and the compatibilizer/clay ratio (Bousmina, 2006; Spencer et al., 2010; Chrissopoulou and Anastasiadis, 2011) on the dispersion and properties of the resulting nanocomposites. It became evident that the type of mixer, the mixing protocol (Cho and Paul, 2001; Dennis et al., 2001; Treece et al., 2007; Médéric et al., 2011) and the operating conditions (Dennis et al., 2001; Lertwimolnun and Vergnes, 2006, 2007; Domenech et al., 2012) strongly influence the dispersion levels attained. In the case of twin-screw extrusion, Vergnes et al. (Lertwimolnun and Vergnes, 2006, 2007; Domenech et al., 2012) showed that even though the extrusion conditions (screw speed, feed rate and temperature) have little impact on intercalation, they influence the final exfoliation levels, which are favoured by high screw speeds (N) and low feed rates (Q). A balance between mechanical shear and residence time is required to achieve proper dispersion (Cho and Paul, 2001; Dennis et al., 2001; Bousmina, 2006; Treece et al., 2007; Lertwimolnun and Vergnes, 2006, 2007; Domenech et al., 2012).

Clay dispersion in the polymer melt encompasses the diffusion of the polymer chains within the clay interlayer spacing (intercalation), the delamination of the individual platelets (exfoliation) due to the application of mechanical stresses, and their diffusion into the melt (Dennis et al., 2001; Bousmina, 2006). The role of the process parameters on the onset and kinetics of these steps has been the subject of debate. Bousmina (2006) coupled an X-Ray instrument to a rotational rheometer and showed that the diffusion of the polymeric chains inside the clay galleries is best obtained under mild shearing conditions (or in a medium to low viscosity matrix) applied during sufficient time, whereas extensive exfoliation requires a high level of shearing/deformation. Understandably, the evolution of clay dispersion along the axis of an extruder, where a complex non-isothermal 3D flow develops, seems less well understood. Lertwimolnun and Vergnes (2006) characterised post-mortem samples removed from various locations along a co-rotating twin screw machine. Based upon previously proposed correlations between rheological response and dispersion levels of nanocomposites, they concluded that both intercalation and exfoliation could reach relatively high levels immediately after melting, and that less restrictive screw profiles yielded better dispersion levels. Furthermore, depending on the combination of screw profile and operating conditions, dispersion could develop, remain constant, or apparently revert along the screw axis, the latter being attributed to matrix degradation even if no experimental evidence of the latter was provided. The degradation of the clay surfactant triggers chain scission reactions on the polymer matrix (Xie et al., 2001; Nassar et al., 2005; Shah and Paul, 2006). For example, Xie et al. (2001) showed that the unsaturated olefins originated from degradation of the alkyl tails of the clay surfactant may cause unfavourable plasticisation of the matrix, thus explaining the unexpected decrease in viscosity of some nanocomposites in comparison with that of the matrix.

Consequently, although global correlations between processing conditions and final dispersion levels have been proposed, the development of dispersion is complex, making more difficult practical process set-up, optimisation and scale-up. The analysis of post-mortem samples removed from the extruder is complex and time consuming. It could also eventually induce thermal degradation and/or morphology changes during material collection and/or sample preparation (e.g., compression moulding of the post-mortem samples into disks, followed by re-heating prior to rheological testing). Therefore, the use of on-line or in-line monitoring techniques to follow the evolution of clay dispersion along the extruder axis seems particularly useful.

The authors developed and validated a prototype on-line oscillatory rheometer (Mould et al., 2011) that, when operated in small amplitude oscillatory shear (SAOS) mode, is capable of measuring rheological parameters such as the storage and loss moduli (G', G'') and melt yield stress (σ_0), which have been correlated with the degree of dispersion (Tanoue et al., 2004; Lertwimolnun and Vergnes, 2006; Shah and Paul, 2006; Xu et al., 2009; Mould et al., 2011; Domenech et al., 2012). The device was able to discriminate the rheological response of a Polypropylene/ Polypropylene grafted with Maleic Anhydride/Organo-Montmorillonite (PP/PP-g-MA/D67G) composite at several locations along the extruder (Mould et al., 2011). An in-line Near-Infrared (NIR) spectroscopy set-up using a diffuse reflectance probe has also been made available. Using adequate chemometrics, the absorbance spectra acquired was related to dispersion level via a 7-parameter model, which combines four rheological parameters (G', G'', σ_0 and a power law index), two Fourier transformed-Infrared spectroscopy (FT-IR) parameters (wavenumber shifts for the peaks at $1050\ \mathrm{cm}^{-1}$ and $1080\ \mathrm{cm}^{-1}$, usually associated to intercalation and exfoliation, respectively (Yan et al., 1996; IJdo et al., 2006; Cole, 2008)) and a thermomechanical index related to the mechanical energy input to the system (specific mechanical energy, SME) (Barbas et al., 2012). The probe was used for real-time in-line monitoring of the preparation of the PP/PP-g-MA/D67G system under different throughputs, the results correlating well with the experimental off-line characterisation measurements. Thus, online rheometry and in-line NIR can be used to characterise samples collected at several locations along the extruder during normal process operation. This avoids subjecting the material to subsequent thermal cycles and, therefore, eliminates one of the possible causes that could explain the apparent reversal of dispersion.

This work uses these two techniques to monitor the evolution along the extruder of the dispersion of a PP/PP-g-MA/D67G system. Three screw profiles with distinct restrictive character are used under constant processing conditions. The morphology of the nanocomposites is observed via scanning transmission electron microscopy (STEM) and X-ray diffraction (XRD), and the degradation effects are analysed by thermal gravimetric analysis (TGA) and time of flight-secondary ion mass spectrometry (TOFSIMS). Reversibility of intercalation was observed along the second half of the extruder, having been originated by the degradation of the organoclay surfactant followed by chain scission of the polymer backbone.

Experimental

Materials

The materials used are identified in Table 1. They include an injection moulding grade Polypropylene (PP), a Polypropylene grafted with Maleic Anhydride (PP-g-MA) to function as compatibilizer and Dellite 67G (D67G), a natural montmorillonite clay modified with dimethyl dihydrogenated tallow quaternary ammonium salt (2 M 2 HT). It has a cation exchange capacity of 115meq/100 g and the dry particle sizes are between 20 and 40μm (Zouari et al., 2012). The PP/PP-g-MA/D67G composition was kept constant at 90/5/5% in weight. The organoclay was dried overnight in a vacuum oven at 80°C, before compounding.

Table 1
Materials used in the work.

Material	Acronym	Producer	Grade	MFI/lamellar distance
Polypropylene	PP	Lyondell Basell	Moplen HP500N	12 g /10 min(230°C /2.16 kg)
Compatibilizer	PP-g-MA	Crompton	Polybond 3200	115 g /10min(190°C /2.16 kg)
Montmorillonite clay	D67G	Laviosa	Dellite 67G	d_{001} = 3.70 nm

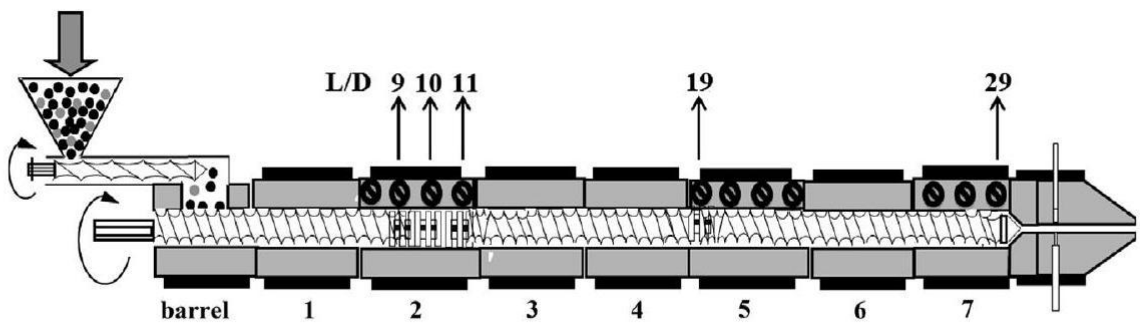

Fig. 1. Layout of the twin-screw extruder.

Table 2
Screw profiles used in the preparation of the PP/PP-g-MA/D67G nanocomposites.

Screw Profile	1	60R/60R4/45R2/30R2/4KD + 60°/5KD90°/4KD − 60°/30R4 L/30R/30R4/20R2/6KD90°/20R4 L /45R/30R/30R2
	2	60R/60R4/45R2/30R2/13KD-30° /20R4/30R/30R4/20R2/6KD90 ° /20R4L/45R/30R/30R2
	3	60R/60R4/45R2/30R2/13KD90° /30R4L/30R/30R4/20R2/6KD90 ° /20R4L/45R/30R/30R2

Table 3
Process monitoring parameters registered during compounding.

	Melt temperature (°C)						Residence time (s)		SME ($Akgh^{-1}$)
	L/D 9	L/D 10	L/D 11	L/D 19	L/D 29	Die	L/D 11	Die	
SC1	(a)	194.0 ± 0.6	198.2 ± 1.4	204.9 ± 0.8	198.9 ± 0.5	207.9 ± 0.4	27 ± 2.0	138 ± 3.0	3.00
SC 2	198.7 ± 0.4	202.6 ± 0.5	(b)	207.8 ± 0.3	199.1 ± 0.4	212.0 ± 0.3	(b)	149 ± 2.6	2.78
SC 3	189.4 ± 0.3	198.5 ± 0.2	203.8 ± 1.3	208.9 ± 0.2	200.2 ± 0.3	211.9 ± 0.4	23.7 ± 0.6	148.7 ± 2.1	2.89

(a) Melting is not completed.
(b) Partially filled screw channels.

Preparation of the nanocomposites

The nanocomposites were prepared in a Leistritz LSM 30.34 modular co-rotating intermeshing twin-screw extruder under fixed operating conditions (100rpm, 3 kg/h and uniform barrel/ die temperature set to 200°C).

The extruder layout is shown in Fig. 1. Three screw profiles (coded as SC1, SC2 and SC3) were utilised, following solutions that are commonly used in the literature on in industrial practice Their construction is presented in Table 2, where $xxRy$ denotes a conveying element (xx being the pitch (mm) and $R = 120/y$ being the length (mm)), $xxKDy^{\circ}$ is a kneading block (xx is the number of individual discs (KD) and y° is their staggering angle) and $xxRyL$ is a left-handed element (L standing for the pitch (mm)). Each screw contains two mixing blocks in between arrays of conveying elements. The geometries differ in the configuration of the mixing block upstream, where polymer melting and a significant contribution to clay intercalation and exfoliation are expected to take place. SC1 and SC3 contain 13 disks followed by a left handed element, while the latter is not present in SC2. In the case of SC1, the first 4 disks are staggered positively, the following 5 are neutral and the last four are staggered negatively. Thus, this geometry should gradually create higher hydrodynamic stresses. The mixing block of SC2 is highly restrictive, but it does not include a left handed element. SC3 consists of 13 disks staggered at 90° (this geometry being usually associated to distributive mixing) followed by a left handed element. The extruder was fitted with modified barrel segments (Fig. 1-barrel segments 2, 5 and 7) designed to allow for material sampling and/or on-line measurements, as explained in more detail below. The use of sample collecting devices made possible a local visual check of the presence of solid vs. molten material, operation under full vs. partial channel filling, measurement of the average melt temperature (by sticking a fast response thermocouple in the freshly collected melt) and estimation of the minimum residence time (by counting the time elapsed between feeding a pigment tracer into the screws and identifying a local colour change in the melt stream).

These will demonstrate the practical effect of the geometrical differences between the screws.

As seen in Table 3, up to $L/D = 11$ (this location corresponds approximately to the downstream edge of the mixing blocks for SC1 and SC3-see also Fig. 1, that of SC2 being shorter), differences in the rate of melting, melt temperature and residence time are more dramatic, then fading towards the die exit. As expected, melting is delayed in screw SC1 and so is melt temperature build up. Local and global residence times seem higher. Conversely, SC2 melts the polymer quickly and causes a significant melt temperature raise. Since its upstream mixing block is shorter, the screws work partially filled at $L/D = 11$ and local melt temperature and residence times measurements were not possible. SC3 seems to induce the same melting as SC2, but the melt temperatures up to $L/D = 11$ are lower (but higher than those for SC1). Therefore, SC1, SC2 and SC3 should create distinct thermomechanical stresses, and thus influence the diffusion and shearing processes in clay dispersion.

Sample collection and on-line/in-line monitoring

At each sampling location identified in Fig. 1, material from the plasticating chamber can flow outwards through lateral channels machined in the barrel wall. A rotating valve diverts the sample to a chamber for sample collection (or temperature measurement), or to the on-line rheometer.

The on-line rheometer prototype set-up uses a DSR301 rheometer head (Anton Paar) and has been validated and described in detail elsewhere (Mould et al., 2011). When measurements are to

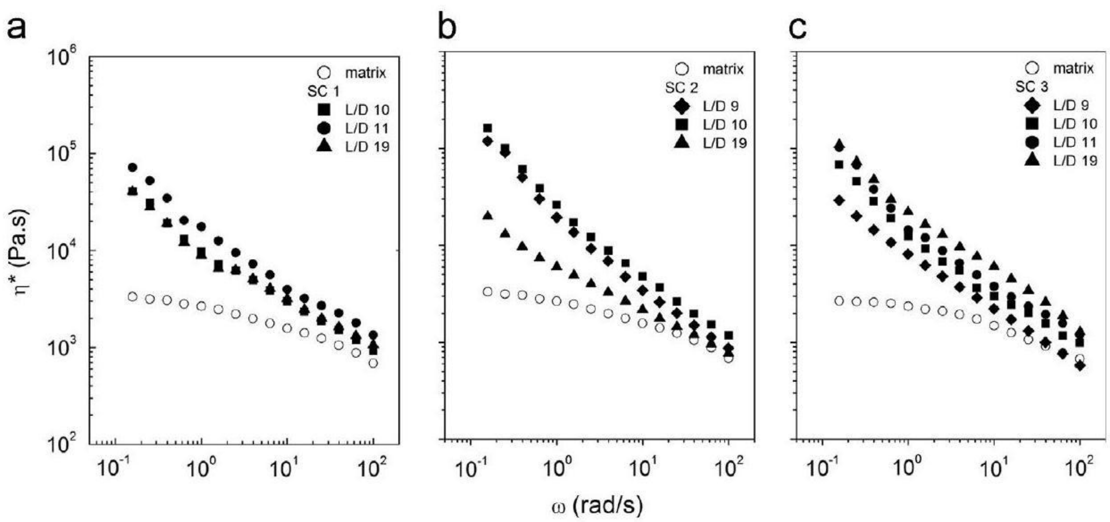

Fig. 2. Complex viscosity (η^*) at several barrel locations for screw profiles (SC): (a) SC1, (b) SC2 and (c) SC3.

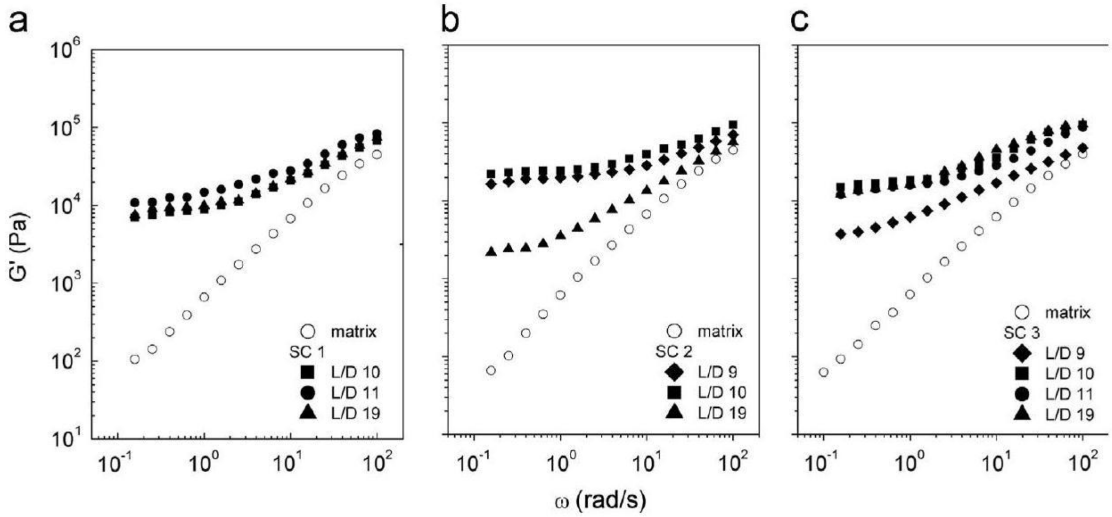

Fig. 3. Storage modulus (G') at several barrel locations for screw profiles: (a) SC1, (b) SC2 and (c) SC3.
be performed, the rotating valve is actuated to divert melt from within the extruder into the measuring chamber at low shear rate, in order to avoid any changes in morphology upon collection. The temperature inside the test chamber is controlled by means of a thermocouple embedded in the lower plate. Sample collection takes about 30 s , corresponding to a cycle of purging, collection and setting the gap, followed by thermal stabilisation at the test temperature. Measurements were performed at $L/D = 9{,}10{,}11$ and 19 (see Fig. 1). They consisted of isothermal (at $200^{\circ}\mathrm{C}$) frequency sweeps from 0.1 to $100 \mathrm{rad/s}$, using parallel plates with a diameter of 20 mm and a 1 mm gap, under a constant strain (1% for the PP matrix and 0.5% for the nanocomposites).

A NIR spectroscopy diffuse reflectance probe (from Hellma Analytics) with a sapphire window (with a diameter of 5.7 mm , for an illuminated area with a diameter of 2 mm and a field depth of 3 mm) was directly fixed to the extruder at $L/D = 9{,}10{,}11{,}19{,}29$ and die body by a Dynisco-type thread. The probe contacts directly the melt stream, no modifications to the extruder or die being necessary. The connexion with the NIR spectrometer (Matrix F, Bruker Optics) is made by fibre optic cables. The NIR spectra were measured from 12000 to $4500 \mathrm{~cm}^{-1}$ with a resolution of $8 \mathrm{~cm}^{-1}$ and accumulation of 4 scans, the acquisition time for each spectrum being approximately 2 s . The background signal is acquired prior to installation, using a Spectralon ® diffuse reflection standard target (Bruker Optics) with a reflectivity index of 99%. Details on the set-up, operation and validation can be found in Barbas et al. (2012). At each location, a total of 50 spectra were measured during regular intervals of continuous extrusion runs. The NIR spectra discussed throughout this work are averages of these, without performing any further processing or signal correction.

Off-line characterisation of the composites

Electron microscopy

Scanning transmitted electron microscopy (STEM) observations of the composites were performed with a NanoSEM Nova200 (FEI), using an acceleration voltage of 15 kV . Ultrathin sections of approximately 80 nm were cut from samples collected from the extruder under cryogenic conditions ($-60^{\circ}\mathrm{C}$), using a UC6 ultramicrotome (Leica) equipped with a diamond knife.

X-ray diffraction

The X-ray diffraction (XRD) patterns were obtained using a diffractometer AXS Nanostar-D8 Discover (Bruker) equipped with a CuK α generator ($\lambda=1.5404 Å$) at 40 kV and 40 mA , in a 2θ range from 0.08° to 10°. The organoclay was analysed directly ($\theta=1.82^{\circ}$, $d_{001}=2.42\ \mathrm{nm}$), whereas the nanocomposite samples were previously compression moulded into disks with a diameter of 20 mm and a thickness of 4 mm .

Medium FT-IR

The FT-IR analyses were performed with a spectrometer FTIR4100 (Jasco). The organoclay was analysed with a KBr mortar. The nanocomposite samples were compression moulded at $200^{\circ}\mathrm{C}$ into $\pm 75\mu\mathrm{m}$ thick films and analysed in transmission mode, in the $4000-500\ \mathrm{cm}^{-1}$ wavenumber range with a resolution of $4\ \mathrm{cm}^{-1}$, using 32 scans. To eliminate interferences due to preferential orientation of the clays (Yan et al., 1996; IJdo et al., 2006; Cole, 2008), the beam was polarised using a KRS-5 grid polarizer lens (SPECAC). At least 3 films were analysed per sample. The wavenumber accuracy and repeatability of the instrument were checked prior to the measurement. The procedure is described in Barbas et al. (2012). Fitting of the Si-O band region (between 1250 and $750\ \mathrm{cm}^{-1}$) (IJdo et al., 2006; Cole, 2008) for the determination of the wavenumber shift for the $1050\ \mathrm{cm}^{-1}$ (Si-O in-plane) and $1080\ \mathrm{cm}^{-1}$ (Si-O out-of-plane) peaks is also described in Barbas et al. (2012).

Thermal gravimetry

Thermal gravimetric analysis (TGA) of the organoclay (D67G), polymer matrix (PP/PP-g-MA 95/5 wt%) and nanocomposites (PP/ PP-g-MA/D67 90/5/5 wt%) were carried out on a Q500 (TA Instruments) under different conditions. Dynamic tests from 50 to $650^{\circ}\mathrm{C}$ used a heating rate of $10^{\circ}\mathrm{C/min}$ under a constant flow of nitrogen ($60\ \mathrm{mL/min}$). The materials were also subjected to isothermal tests at $150^{\circ}\mathrm{C}, 180^{\circ}\mathrm{C}$ and $200^{\circ}\mathrm{C}$ (set processing temperature) for 10 min , under a constant flow of nitrogen ($60\ \mathrm{mL/min}$).

Mass spectrometry

Samples of the matrix, organoclay and nanocomposites were also analysed by Time of Flight-Secondary Ion Mass Spectrometry (TOF-SIMS). A TOF-SIMS IV (Ion-Tof GmbH) equipped with a reflectron TOF-mass analyser (operated at $10^{10}\mathrm{mbar}$), bismuth (Bi_3^{2+}) cluster ion source (25 keV) and a pulsed electron flood source for charge compensation were used. Positive secondary ion mass spectra were acquired over a mass range from $m/z=0$ to 1000. The analysed area of each spectrum is $(152\times 152)\mu\mathrm{m}^2$, with an acquisition time of 30 s per spectrum. The ion dose was kept below the static limit ($10^{12}/10^{13}$ ions $/\mathrm{cm}^2$) and the mass resolution ($m/\Delta m$) of the secondary ion peaks ranged in the interval 45008000.

Results and discussion

Evolution of clay dispersion

The rheological response of polymer-clay nanocomposites (usually measured in SAOS mode) has been extensively used to estimate the degree of dispersion of the organoclay (Tanoue et al., 2004; Vermogen et al., 2005; Lertwimolnun and Vergnes, 2006; Durmus et al., 2007; Cassagnau, 2008; Xu et al., 2009). The increase of the storage (G') and loss (G'') moduli has been generally related to a finer dispersion (Tanoue et al., 2004; Cassagnau, 2008; Xu et al., 2009). The formation of a plateau at low frequencies, which has been attributed to the deformation and recovery of the dispersed solid particles, has been proposed as a measure of exfoliation (Tanoue et al., 2004; Vermogen et al., 2005; Xu et al., 2009). Vergnes et al. (Lertwimolnun and Vergnes, 2006, 2007; Vergnes, 2011) used a modified Carreau-Yasuda model with yield stress to describe the frequency (ω) dependence of the absolute complex viscosity (η^*):

$$|\eta^*(\omega)| = \frac{\sigma_0}{\omega} + \eta_0[1 + \lambda\omega^a]^{(b-1)/a} \tag{1}$$

and successfully related this with the exfoliation level. Alternatively, a power law expression has also been suggested (Vermogen et al., 2005; Durmus et al., 2007):

$$|\eta^*(\omega)| = A\omega^b \tag{2}$$

the exponent (b) being associated with the state of clay dispersion. Figs. 2 and 3 show the variation with frequency of the complex viscosity and storage modulus at various locations along the extruder, for the three different screws. As expected, the nanocomposites exhibit higher viscosity and modulus than the matrix. Also, in all cases, G curves present a plateau at the lower frequency range, suggesting the presence of elastic particles. As for the evolution along the screw, the relative position of the curves at $L/D = 10{,}11$ and 19 clearly depends on screw geometry. It is evident that η^* and G' do not always increase as the material progresses in the screw, which would correspond to a gradual dispersion.

Fig. 4 shows the rheological data as a function of axial length (at a constant frequency) in terms of storage modulus (G ') and yield stress (σ_0). Generally, dispersion progresses until $L/D = 11$, i.e., along the first kneading block, decreasing more or less significantly thereafter. Identical results were obtained by off-line rheometry measurements (not shown). The axial variation of G' and σ_0 is relatively similar for SC1 and SC3, but in the case of SC2 not only the initial values are higher, but the subsequent decay is more pronounced. Table 3 shows that this profile induced higher melt temperatures in the mixing block upstream ($L/D = 9$ and $L/\,D = 10$) and a total residence time similar to that of SC3, which generated lower melt temperatures at the same mixing block.

Fig. 5 displays the in-line NIR spectra obtained for the same axial locations, plus $L/D =$ 29 and die body (where on-line rheometry was not possible). The vertical shift upwards of the baseline in reflection has been associated with dispersion (Barbas et al.,

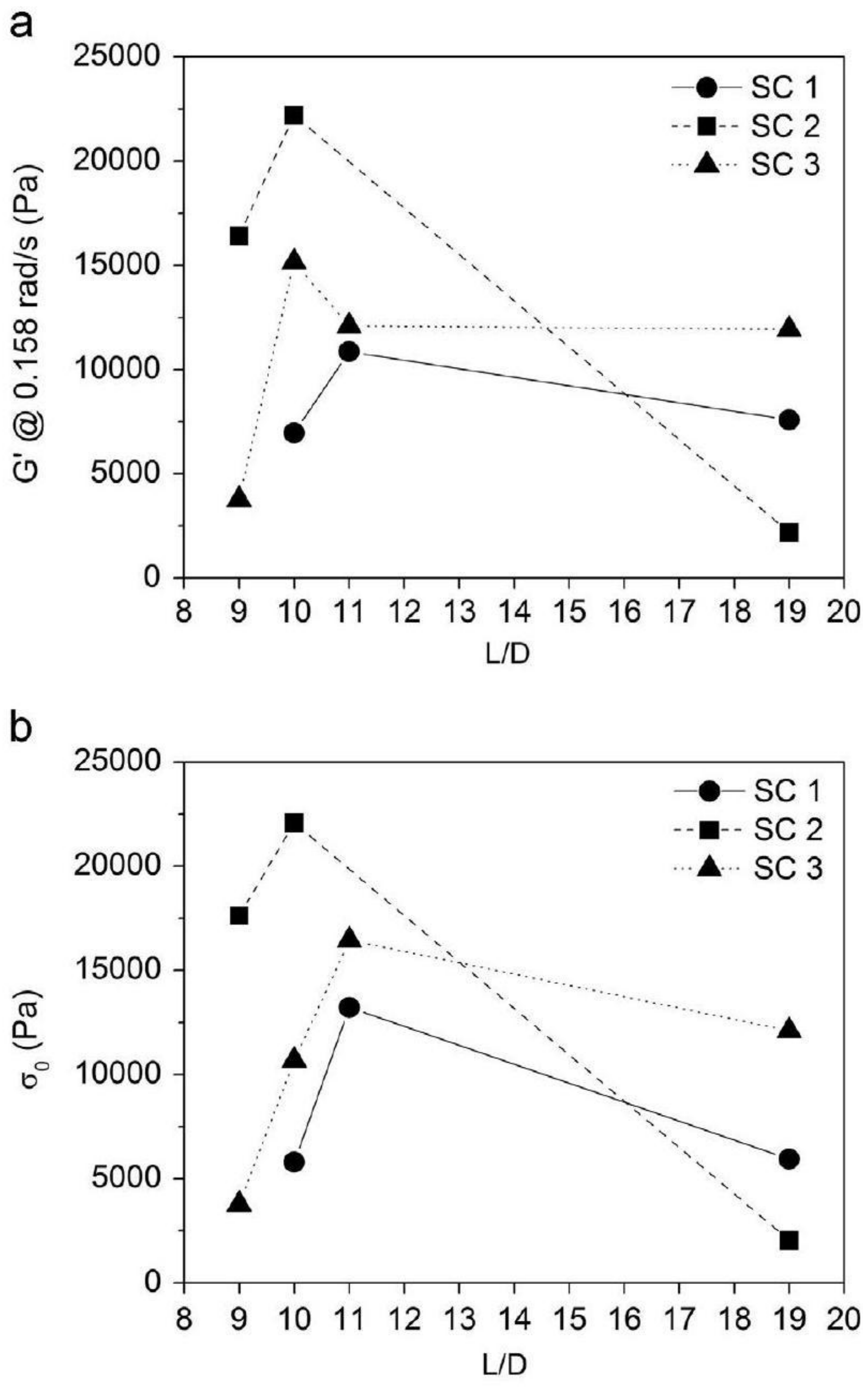
a
G' @ 0.158 rad/s (Pa)
L/D
SC 1
SC 2
SC 3
b
σ_0 (Pa)
L/D
SC 1
SC 2
SC 3

Fig. 4. Storage modulus (G') and yield stress (σ_0) along the extruder for the different screw profiles (SC).

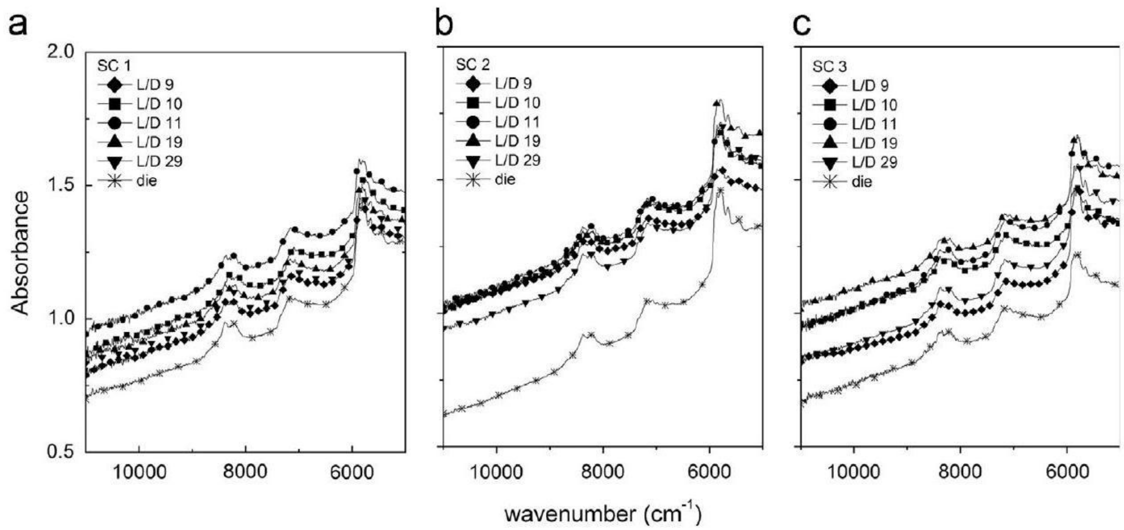

Fig. 5. NIR spectra along the extruder barrel for the different screw profiles: (a) SC1, (b) SC2 and (c) SC3.

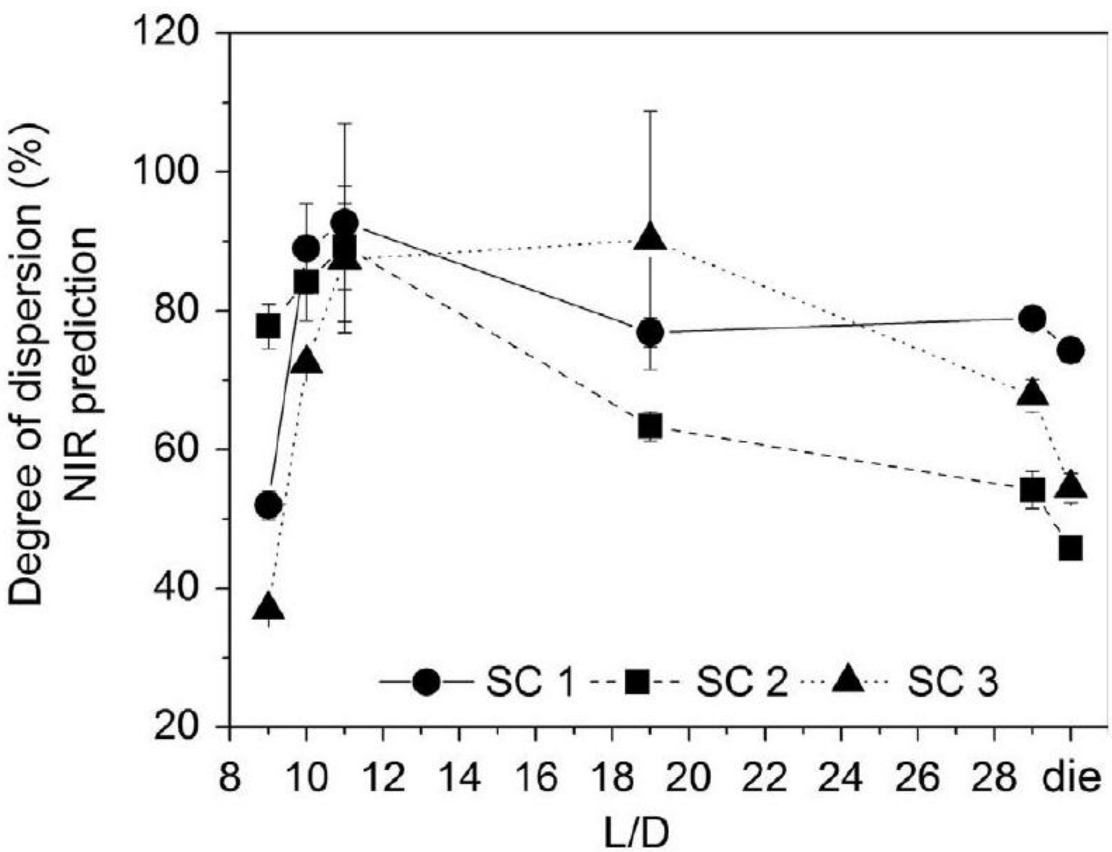

Fig. 6. NIR real-time predictions of the degree of dispersion along the extruder. 2012), since a larger number of particles (clay stacks and/or individual platelets) with smaller sizes and higher inter-lamellar distance enhance the light scattering effects. For all screw profiles, this occurs from $L/D=9$ to $L/D=11$ or 19 , and then shifts downwards at $L/D=29$ and/or die, i.e., reversion of dispersion seems to be taking place downstream. Using chemometrics, in-line NIR data can be linked to dispersion in a more precise way, relating the spectral differences with reference parameters often used to assess clay dispersion. The model used here was developed based on samples with variable clay loading and compatibilizer content and processed under different screw speeds and outputs (Barbas et al., 2012). It incorporates 7 parameters extracted from oscillatory rheometry (G', G'', σ_0, b-see Eqs. (1) and (2)), FT-IR (wavenumber shift of the peaks at 1050 and 1080 cm^{-1}) and a process-related thermomechanical index, specific mechanical energy (SME). The quality of the NIR predictions is assessed by the Root Mean Square Error of Prediction (RMSEP) and bias (Barbas et al., 2012). The predictions shown in Fig. 6, plotted as a function of extruder location, are extrapolated from a calibration curve developed at L/D 11 (Barbas et al., 2012), therefore yielding higher global errors (RMSEP of 14.1 for SC1, 5.1 for SC2 and 15.6 for SC3) and bias (5.1 for SC1, 1.1 for SC2 and 5.8 for SC3). The evolution presented is consistent with that in Fig. 4. For all screw profiles, dispersion evolves fast along the first mixing zone ($L/D=9-11$) and then beyond $L/D=11$ it either remains roughly constant or regresses. As before, reversibility is more significant for SC2.

Therefore, using the customary rheology (SAOS) and NIR parameters to estimate dispersion, it may be concluded that a more or less pronounced reversion of dispersion seems to occur along the second half of the extruder (beyond $L/D=11$). In the case of on-line rheology data, thermo-oxidative degradation of the matrix, platelet alignment or local lubrication effects, could eventually account for the decrease of the values of the rheological parameters. Also, NIR is sensitive to orientation interferences due to the trichroic nature of the clay (Yan et al., 1996; IJdo et al., 2006). However, the possibility of an effective reversion step in the dispersion mechanism of organoclays should be considered.

Reversion as a step of dispersion?

Fig. 7 shows the XRD patterns of the nanocomposites for all screw profiles at several axial locations. In comparison with the organoclay peak position, the results reveal a shift of the diffraction peak to lower angles for all screw profiles up to $L/D=11$, confirming the increase of the interlayer d-spacing. At $L/D=10$, the interlayer d-spacing is highest for SC2 and lowest for SC1, which is in agreement with the on-line rheology data (Fig. 4). However, from $L/D=19$ onwards the peak shifts to higher angles, indicating a decrease of the interlayer d-spacing. These results confirm the likelihood of reversion of dispersion during the second half of the extruder, which seems to be more pronounced for screw SC2. Fig. 8 displays STEM micrographs of samples collected along the extruder, prepared with screw SC2, with the same magnification. The dark traces correspond to the clay platelets. Intercalated structures can be generally observed, but it appears that the platelet size increases from $L/D=19$ onwards, until the die exit. It seems as if some clay re-aggregation is taking place, i.e., the dispersion achieved in the first mixing zone is partially lost.

As referred above, the FT-IR spectra of organoclays and resulting nanocomposites show a pronounced band between 1250 and 750 cm^{-1} due to the Si-O bonds of the silicate. It has been suggested (Yan et al., 1996; IJdo et al., 2006; Cole, 2008) that this band can be decomposed in at least four peaks, three being related to the Si-O in-plane vibrations appearing at about 1120, 1050 and 1020 cm^{-1}, and the fourth to the $Si - O^{-}$out-of-plane vibration appearing at about 1080 cm^{-1}. As individual clay layers become more spaced, the peaks at 1050 cm^{-1} and 1080 cm^{-1} tend to shift. Consequently, the negative peak shift at 1050 cm^{-1} has been related to the penetration of the polymer chains inside the clay galleries (intercalation), whilst the positive shift of the peak at 1080 cm^{-1} is attributed to the delamination of the clay platelets (exfoliation) (IJdo et al., 2006; Cole, 2008). Fig. 9 shows the evolution along the extruder axis of these peak shifts for the system under study and the three screw profiles. Up to $L/D = 11$, the development of intercalation (Fig. 9a) is coherent with the

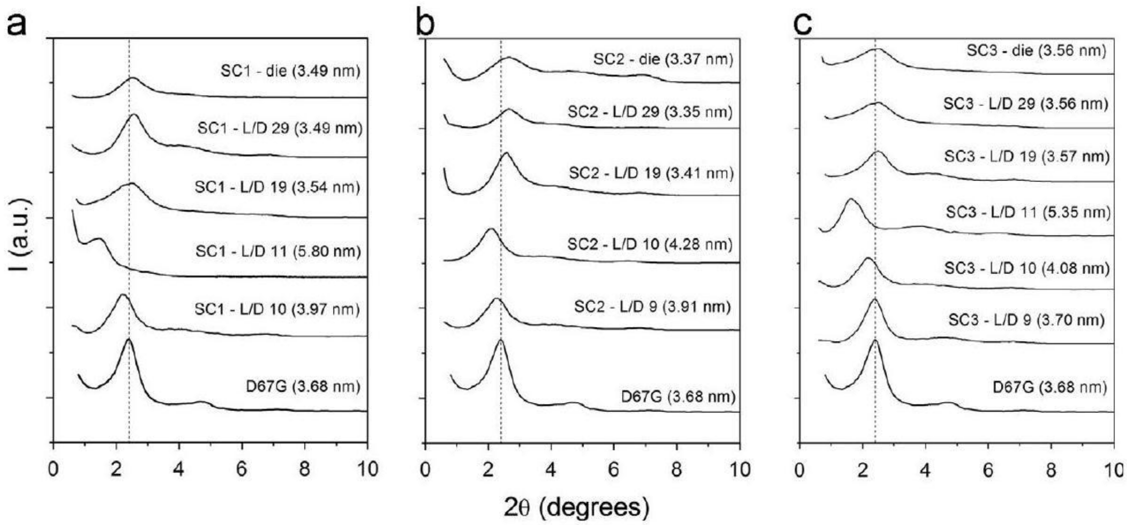

Fig. 7. XRD patterns for the samples collected along the extruder: (a) SC1, (b) SC2 and (c) SC3.

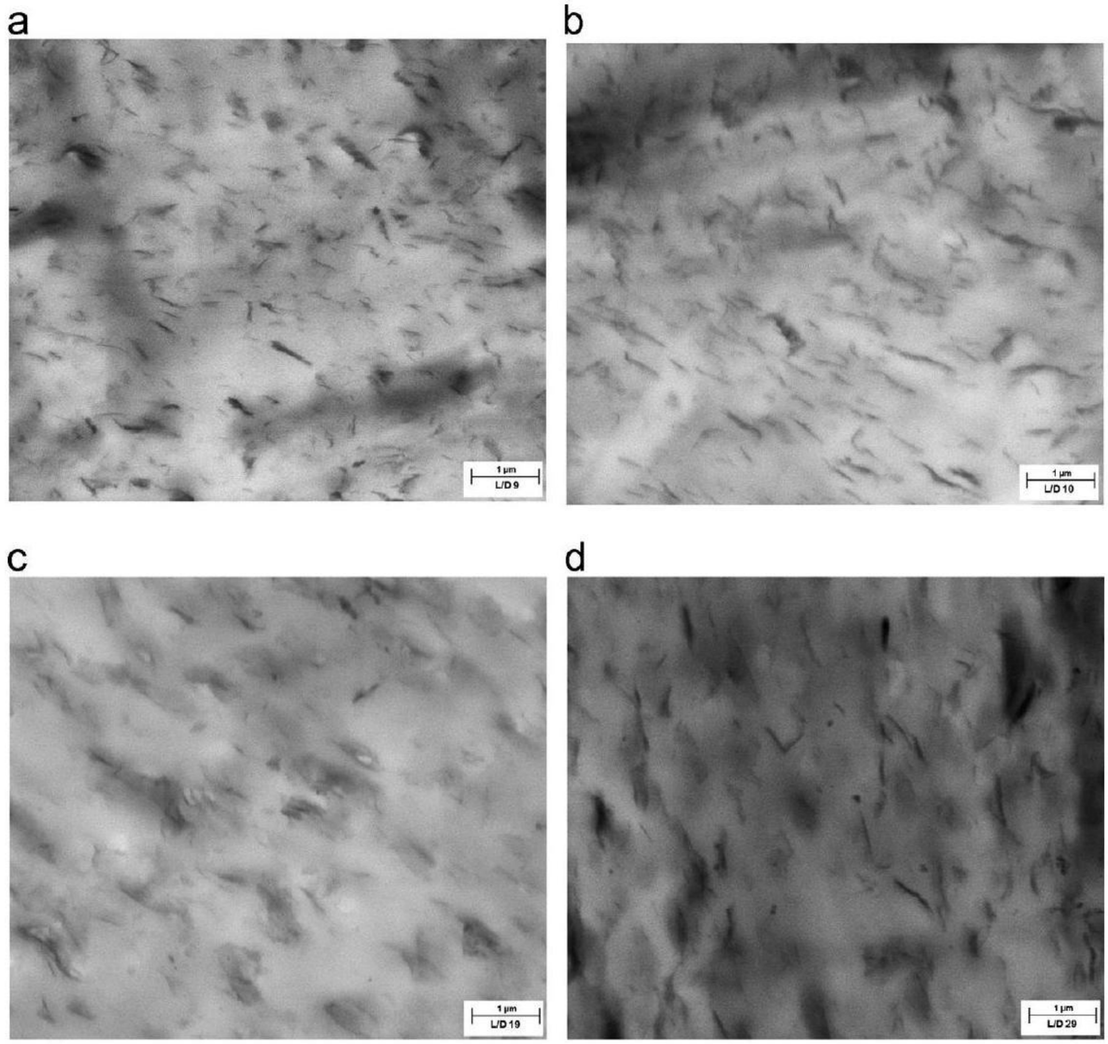

e

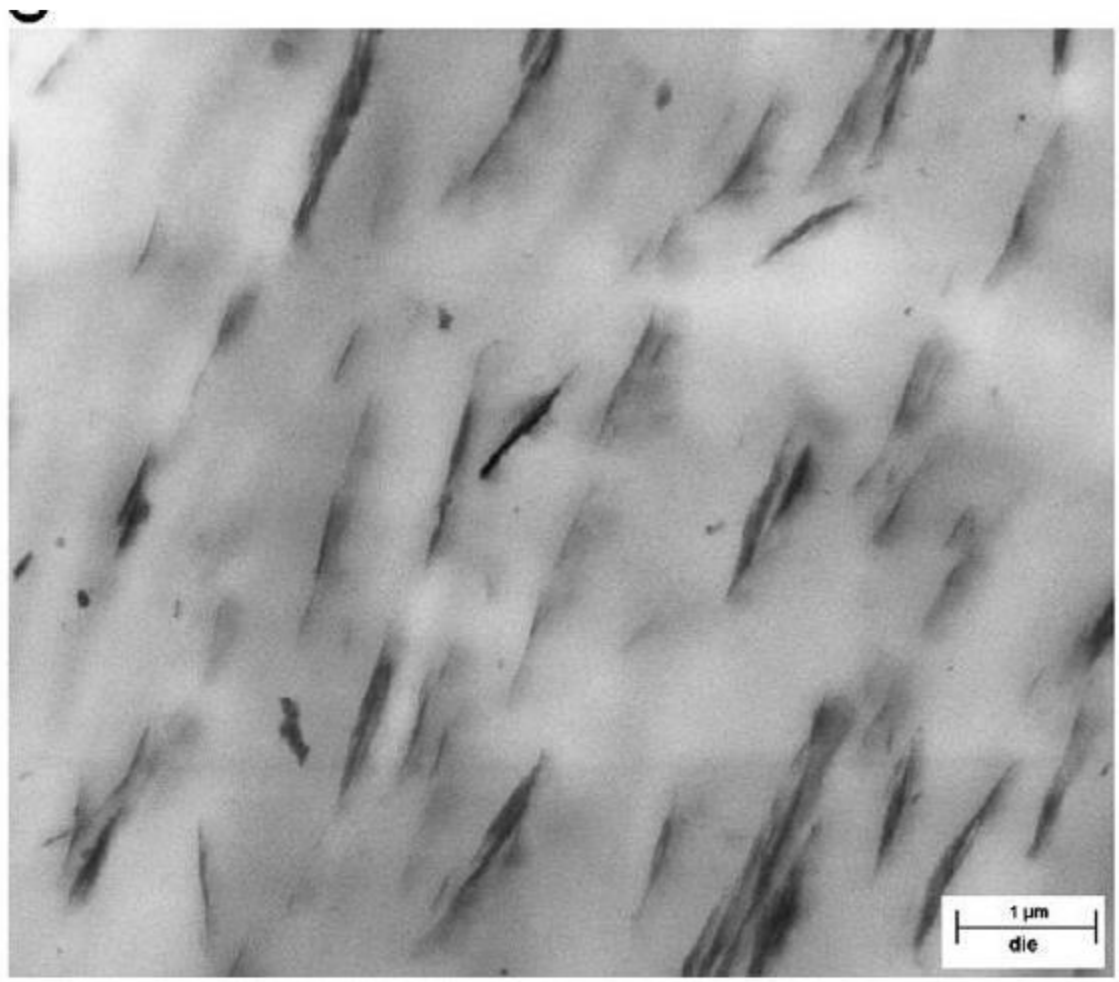

Fig. 8. Morphology of the nanocomposites prepared with SC2 profiles at several axial locations.

dispersion determined by in-line NIR (Fig. 6). At $L/D = 19$, the FT-IR peak shifts for SC1 and SC2 are different from the evolution given by the other techniques. At the die, both NIR and FT-IR show again similar trends and indicate that reversion occurred. This partial discrepancy of the FT-IR data at $L/D = 19$ is not easy to explain, but could be a consequence of the small size of the samples used by

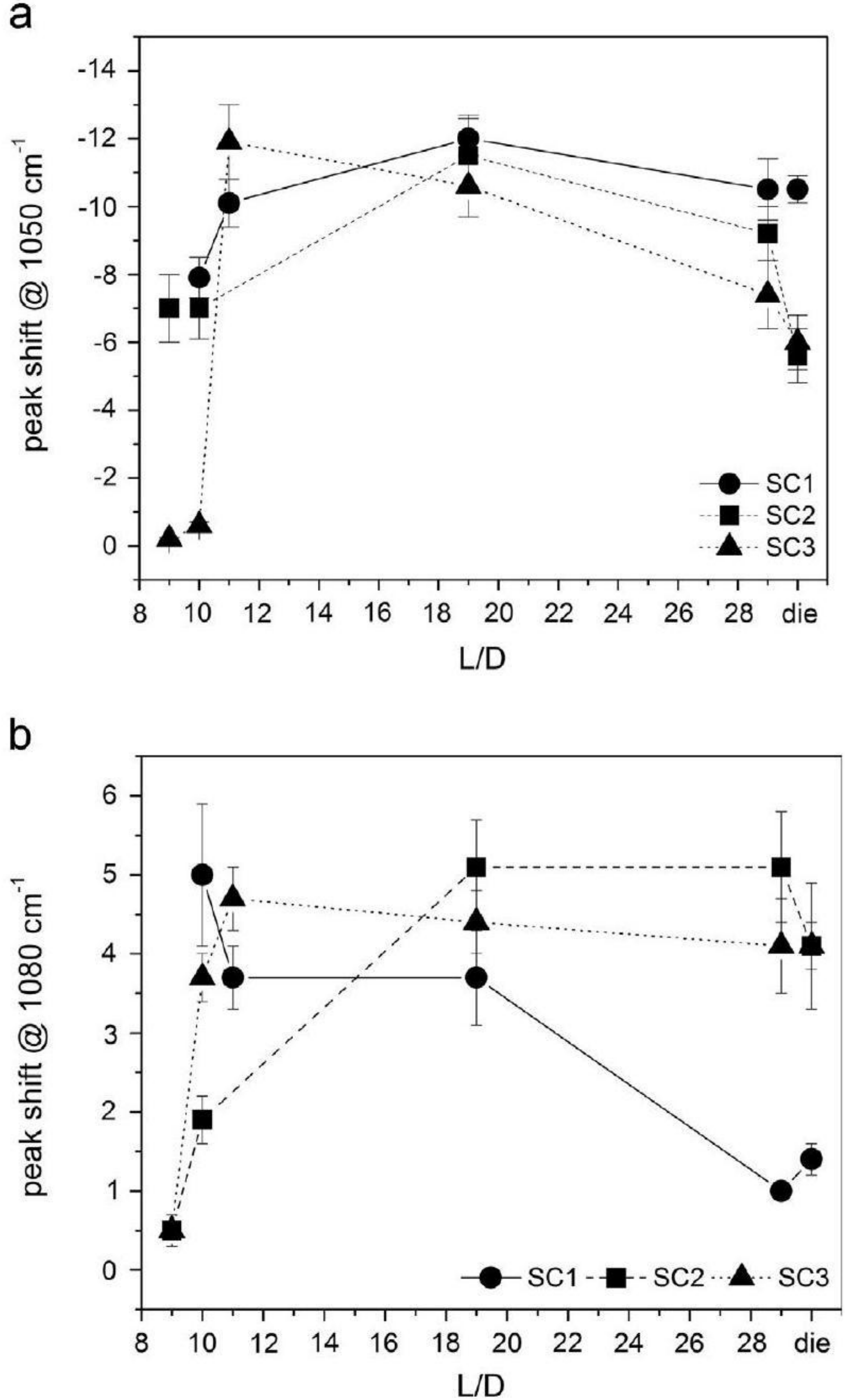
a
peak shift @ 1050 cm^{-1}
-14
-12
-10
-8
-6
-4
-2
0
8
10
12
14
16
18
20
22
24
26
28
die
L/D
SC1
SC2
SC3
b
peak shift @ 1080 cm^{-1}
6
5
4
3
2
1
0
8
10
12
14
16
18
20
22
24
26
28
die
L/D
SC1
SC2
SC3

Fig. 9. FTIR analysis: (a) in-plane peak ($1050\ cm^{-1}$) shift; (b) out-of-plane peak ($1080\ cm^{-1}$) shift.

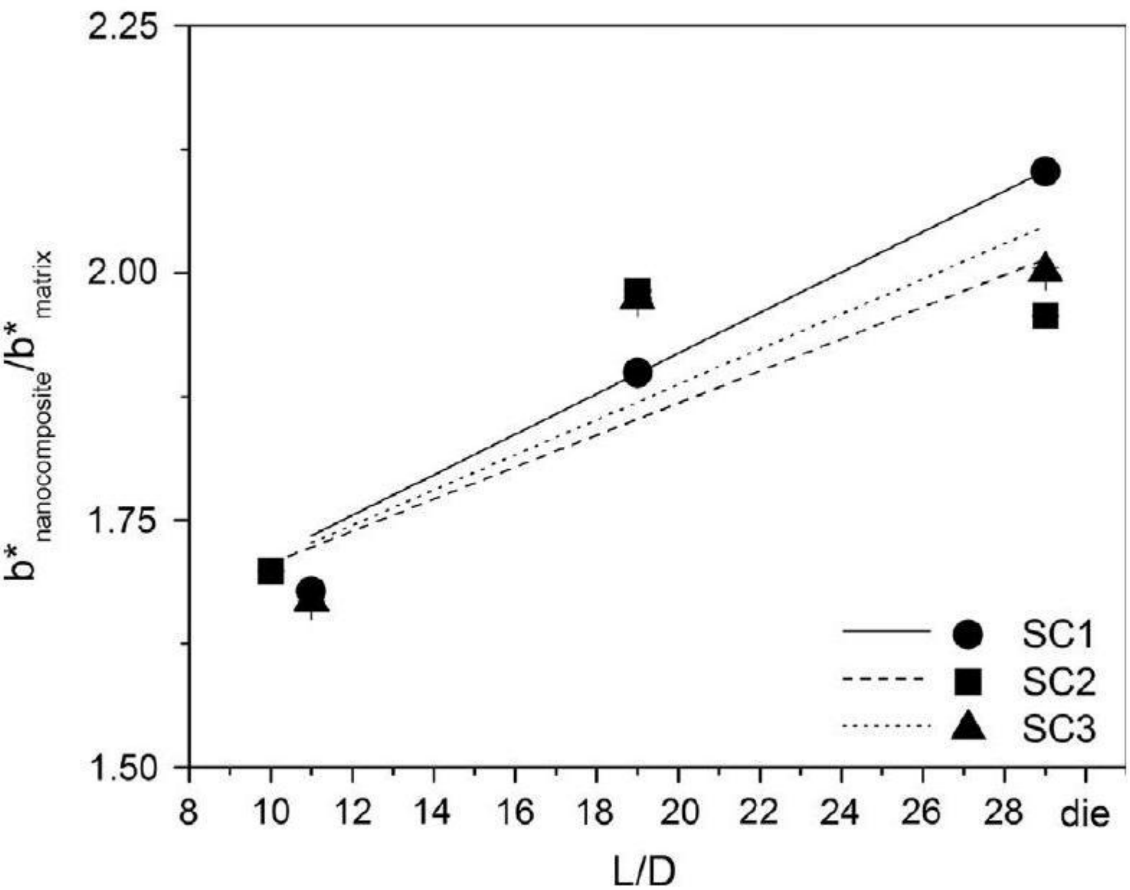

Fig. 10. Yellowness ratio along the extruder for the different screw profiles.
this technique, which may not truly represent the morphology of the material at that location. Generally, exfoliation (Fig. 9b) increased up to $L/D = 11$, in global accordance with the behaviour of the yield stress (Fig. 4b). However, the relative magnitude associated with each screw is different. Also, in the case of SC1 a continuous decrease is observed, which would mean that exfoliation developed very rapidly upstream and is not consistent with the rheological data. Moreover, while the rheological parameters for all screws decrease in the second part of the extruder, FT-IR data only indicates reversion for screw SC1. Therefore, although FT-IR data has the potential to discriminate between intercalation and exfoliation it should be examined with some precaution and be complemented by other techniques.

Up to $L/D = 11$, the relative magnitude of the yield stress (Fig. 4), i.e., the extent of exfoliation, matches the development of average temperature presented in Table 3, the screws ranking as SC2 > SC3 > SC1. Exfoliation is commonly linked to the action of sufficiently high hydrodynamic stresses, but higher temperatures are apparently contradictory, as they induce lower viscosities. Accordingly, the higher local temperatures probably result from the earlier melting onset, and thus from a longer exposure of the freshly molten material to the high stress levels during longer periods. Therefore, the results discussed so far suggest that both intercalation and exfoliation develop quickly along the kneading block upstream. From then onwards the evolution in dispersion is

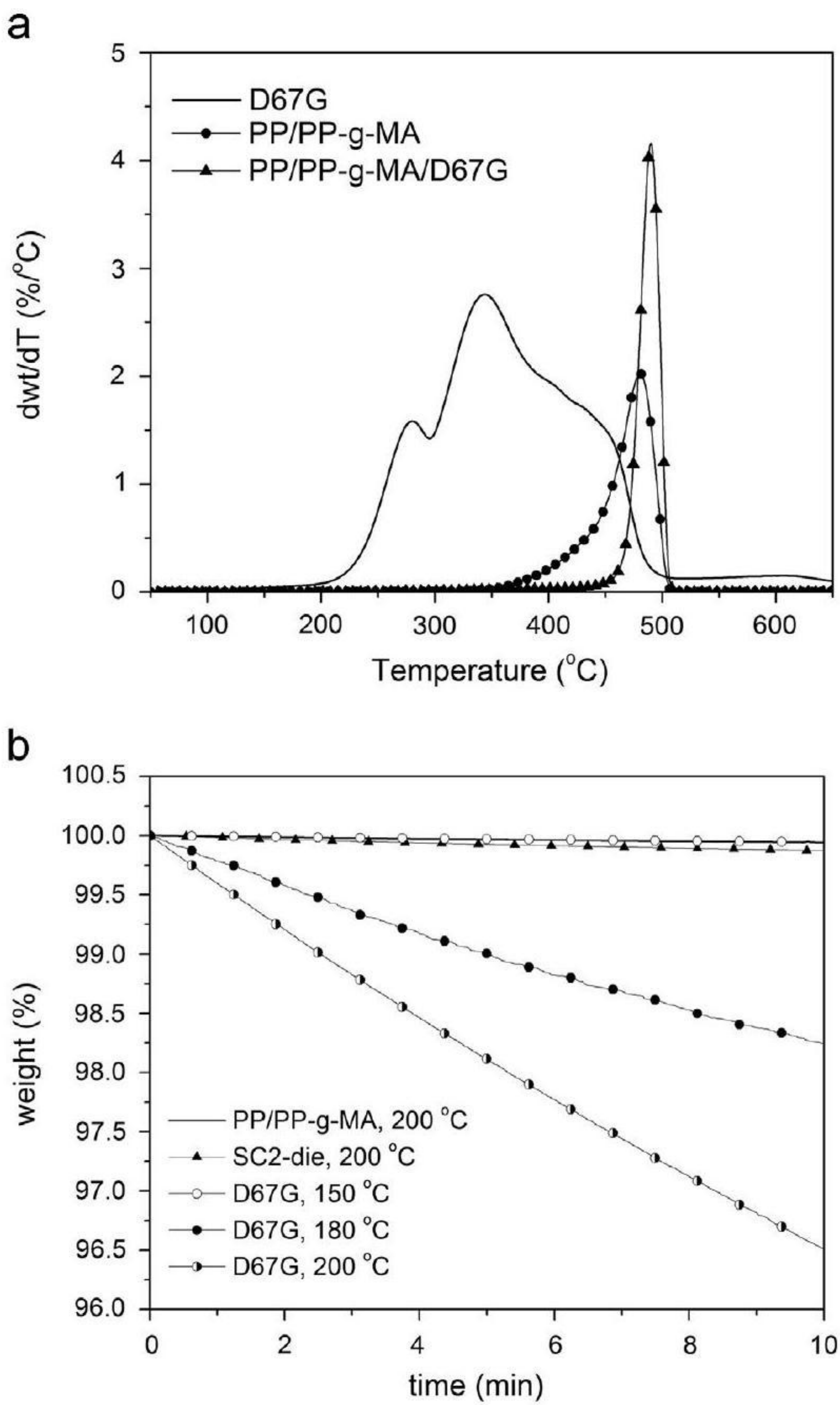

a
D67G
PP/PP-g-MA
PP/PP-g-MA/D67G
dwt/dT (%/°C)
Temperature (°C)
0
1
2
3
4
5
100
200
300
400
500
600
b
PP/PP-g-MA, 200 °C
SC2-die, 200 °C
D67G, 150 °C
D67G, 180 °C
D67G, 200 °C
weight (%)
time (min)
96.0
96.5
97.0
97.5
98.0
98.5
99.0
99.5
100.0
100.5
0
2
4
6
8
10

Fig. 11. TGA results for the organoclay (D67G), polymer matrix (PP/PP-g-MA) and nanocomposite (PP/PP-g-MA/D67G) prepared with SC2: (a) dynamic derivative curves and (b) isothermal curves.

much slower, non-existent, or even some reversion of the process can be detected. Particularly in the second part of the extruder and during flow through the die, re-agglomeration, i.e., decrease of intercalation (and, in some cases, possible re-agglomeration of individual platelets), seem to take place. Despite of this, the final dispersion levels can be quite significant.

Reversion was mostly observed along the second part of the extruder, where the cumulative residence times become important, but the hydrodynamic stresses should be lower than those developing upon melting. Therefore, degradation of the matrix or of the clay surfactant could play a role. Indeed, matrix degradation would entail a decrease of its viscosity, with possible diffusion of the melt out of the clay interlaying spacing, and the eventual collapse of the platelet network; the closer contact between individual platelets could also induce some re-agglomeration. Surfactant degradation lowers both the interlaying spacing and the interaction with the matrix, thus promoting the above phenomena.

The extent of degradation was assessed by TGA and TOF-SIMS. Colour measurements are depicted in Fig. 10 as yellowness ratio along the extruder. The results are similar for the three screws and show the expected increase along the screw length, confirming the incidence of degradation. Still, they cannot discriminate whether the latter would preferentially affect the clay surfactant or the polymer matrix. TGA data is presented in Fig. 11. Significant weight changes start at different temperatures, specifically $246^{\circ}C$ for the organoclay, $444^{\circ}C$ for the matrix and $478^{\circ}C$ for the nanocomposite (Fig. 11a). The isothermal tests (Fig. 11b) reveal that at $150^{\circ}C$ the organoclay suffers a minor weight change (less than 0.05%), but at $180^{\circ}C$ and $200^{\circ}C$ the weight loss increases to 1.8wt% and 3.5wt% respectively, due to the volatilization of lower molecular weight components associated with the decomposition of the alkylammonium modifier. As D67G contains 45% of organic surfactant, at $200^{\circ}C$ all the surfactant is lost. Since the degradation of quaternary ammonium compounds follows a Hofmann elimination reaction, in the specific case of D67G the degradation of the dimethyl dihydrogenated tallow surfactant results in a trimethylamine ($N(CH_3)_3$) and α-olefins (e.g. $CH2 = CH - (CH_2)_n - CH_3$) (Xie et al., 2001; Fornes et al., 2003; Nassar et al., 2005). Similar results were described by other authors (Shah and Paul, 2006; Cui et al., 2009). Conversely, the PP/PP-g-MA matrix and the extruded nanocomposites remain stable during the isothermal tests even at $200^{\circ}C$, with a total weight loss of 0.05% and 0.1%, respectively.

TOF-SIMS was performed on organoclay (D67G) and samples of polymer matrix (PP/PP-g-MA) and nanocomposite, prepared with

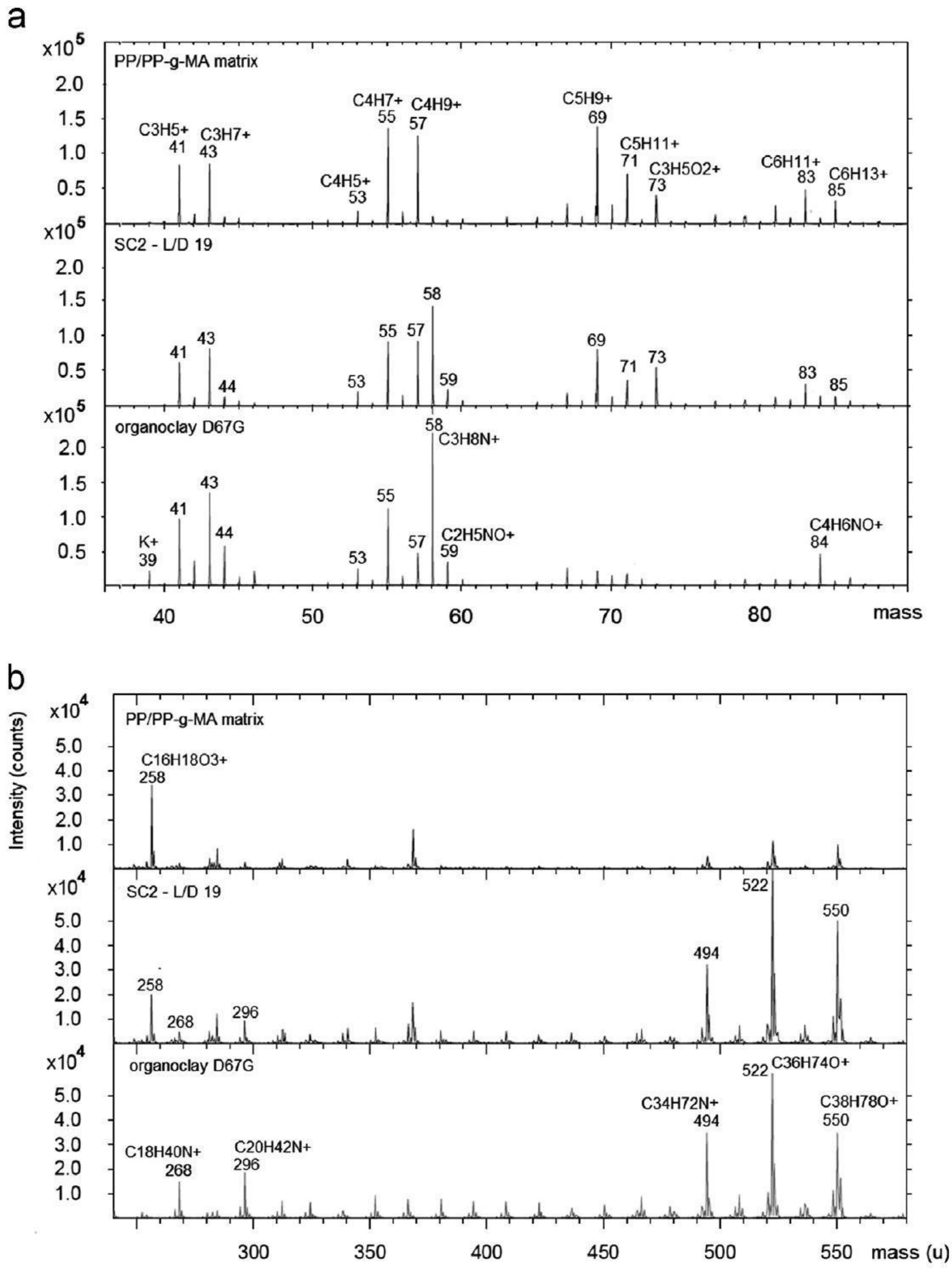

Fig. 12. TOF-SIMS spectra of organoclay (D67G), polymer matrix (PP/PP-g-MA) and nanocomposite (PP/PP-g-MA/D67G) at $L/D = 19$, prepared with SC2: (a) low mass region

and (b) high mass region.
screw SC2 and collected at $L/D = 19$, in order to verify degradation of the polymer matrix. The low and high mass regions of the spectra are depicted in Fig. 12. The major ion fractions in the mass range below 60 amu are attributed to the aliphatic hydrocarbons characteristic of organic compounds ($C_3H_5^+$at 41 amu, $C_3H_7^+$at 43 , $C_4H_5^+$at 53, $C_4H_7^+$at 55 and $C_4H_9^+$at 57 amu). These peaks are present in polypropylene, nanocomposite and organoclay spectra (in this case, they are related to the organic surfactant). From 57 amu onwards, some organic species are only present in the PP/ PP-g-MA matrix and nanocomposite sample, specifically $C_5H_9^+$at 69amu, $C_5H_{11}^+$at 71, $C_5H_{11}^+$at 71, $C_6H_{11}^+$at 83 and $C_6H_{13}^+$at 85 amu . However, the spectrum of the nanocomposite shows a decrease of the relative intensity of these peaks, suggesting degradation of the matrix by chain scission (Galuska, 1997; Awaja et al., 2011). The same spectrum also displays some of the characteristic peaks of the organoclay, explicitly the most intensive rich nitrogen ions from the quaternary alkyl ammonium surfactant (Awaja et al., 2011), such as $C_2H_6\ N^+$(44 amu), $C_3H_8\ N^+$(58), $C_2H_5NO^+$(59), $C_4H_6NO^+$(84), $C_{18}H_{40}\ N^+$(268), $C_{20}H_{42}\ N^+$(296) and $C_{34}H_{72}\ N^+$ (494 amu). Again, the spectrum of the nanocomposite exhibits a decrease of the relative intensity of the respective peaks, plus the increase of the relative intensity of the peaks attributed to oxidation species like $C_{36}H_{74}O^+$(522amu) and $C_{38}H_{78}O^+$ (550 amu) (Awaja et al., 2011), thus confirming degradation of the clay surfactant by Hofmann elimination, followed by β-scission of the long alkyl tails.

Consequently, both thermal degradation of the clay surfactant and polymer matrix seem to contribute to the observed reversion of dispersion along the extruder. The first effect was studied by other authors (Nassar et al., 2005; Shah and Paul, 2006), who concluded that the α-olefins formed by degradation of the alkyl tails of the surfactant readily react with oxygen to form peroxide species, eventually causing chain scission of the polymer matrix. Additionally, the plasticisation effect of these shorter chain hydrocarbons described by Xie et al. (2001) correlates well with the reversion detected by on-line rheometry and in-line NIR. Moreover, the thermo-oxidative degradation of the clay surfactant has a strong influence on the mechanism and extent of dispersion, since by affecting the polymer-clay interface it hinders the diffusion of the polymer melt within the clay layers (Dennis et al., 2001; Bousmina, 2006).

A proper combination of shear and residence time will quickly create high levels of dispersion. Once degradation of the clay surfactant initiates, while the exfoliated layers persist, the intercalated clay stacks re-aggregate. This explains the rheological behaviour of the nanocomposites prepared with screws SC2 and SC3 (Fig. 4), the exfoliation levels detected by FT-IR (Fig. 9b) and the dispersion levels observed by STEM (Fig. 8). When matrix degradation also develops, the resulting decrease in viscosity interferes with the dynamics of dispersion. The hydrodynamic stresses may become insufficient to overcome the cohesive forces between clay layers; the less viscous polymer melt will likely diffuse out of clay galleries or facilitate clay re-aggregation. These phenomena could account for the results obtained with screw SC1, where exfoliation was seen to decrease to almost zero after $L/D = 11$ (Fig. 9b), suggesting that the exfoliated structure could not be supported by the polymer matrix (Fornes et al., 2001; Bousmina, 2006; Xu et al., 2009).

Conclusions

On-line oscillatory rheometry and in-line NIR were used to study the evolution of dispersion during the preparation of a PP/ PP-g-MA/organoclay system by twin screw compounding. Three different screw profiles were adopted. Regardless of the screw profile, a significant contribution to the final dispersion level is provided during the initial process stages, during melting and up to $L/D = 11$. Further downstream, the two techniques indicated that dispersion would level off and/or decrease, even if the final dispersion levels were quite significant. These observations were generally confirmed by STEM, XRD and FT-IR analyses on samples collected from the extruder. TGA and TOF-SIMS demonstrated that degradation of the clay surfactant develops even at low processing temperatures, triggering the subsequent degradation of the polymer matrix.

The results show that a certain level of hydrodynamic stresses and residence time will quickly create high levels of dispersion (intercalation and exfoliation). However, if degradation of the clay surfactant initiates, the intercalated clay stacks re-aggregate. When matrix degradation also develops, the resulting decrease in viscosity will not only reduce the hydrodynamic stresses, which may become too low to overcome the cohesive forces between clay layers, but also allow the polymer melt to diffuse out of clay galleries or facilitate clay re-aggregation.

From a practical point of view, the results generally show that as long as the mixing zones in the screws create enough stresses during sufficient times, geometrical differences are a second order factor, since good dispersion is achieved. Moreover, in terms of mixing there is little advantage in using screws with long L/D ratios, as the corresponding longer residence times, in association with viscous dissipation, will eventually trigger degradation phenomena with the repercussions on dispersion discussed here.

References

Awaja, F., Moon, J.B., Gilbert, M., Zhang, S., Kim, C.G., Pigram, P.J., 2011. Surface molecular degradation of selected high performance polymer composites under low earth orbit environmental conditions. Polym. Deg. Stab. 96, 1301-1309.

Barbas, J.M., Machado, A.V., Covas, J.A., 2012. In-line Near-Infrared spectroscopy: a tool to monitor the preparation of polymer-clay nanocomposites in extruders. J. Appl. Polym. Sci. 127, 4899-4909.

Bousmina, M., 2006. Study of intercalation and exfoliation processes in polymer nanocomposites. Macromolecules 39, 4259-4263.

Cassagnau, P., 2008. Melt-rheology of organoclay and fumed silica nanocomposites. Polymer 49, 2183-2196.

Cho, J.W., Paul, D.R., 2001. Nylon 6 nanocomposites by melt compounding. Polymer 42, 1083-1094.

Chrissopoulou, K., Anastasiadis, S.H., 2011. Polyolefin/layered silicate nanocomposites with functional compatibilizers. Eur. Polym. J. 47, 600-613.

Cole, K.C., 2008. Use of Infrared spectroscopy to characterize clay intercalation and exfoliation in polymer nanocomposites. Macromolecules 41, 834-843.

Cui, L., Bara, J.E., Brun, Y., Yoo, Y., Yoon, P.J., Paul, D.R., 2009. Polyamide and polycarbonate based nanocomposites prepared from thermally stable imidazolium organoclay. Polymer 50, 2492-2502.

Dennis, H.R., Hunter, D.L., Chang, D., Kim, S., White, J.L., Cho, J.W., Paul, D.R., 2001. Effect of melt processing conditions on the extent of exfoliation in organoclaybased nanocomposites. Polymer 42, 9513-9522.

Domenech, T., Peuvrel-Disdier, E., Vergnes, B., 2012. Influence of twin-screw processing conditions on structure and properties of Polypropylene-Organoclay nanocomposites. Int.

Polym. Process. 27, 517-526.
Durmus, A., Kasgoz, A., Macosko, C.W., 2007. Linear low density polyethylene (LLDPE)/clay nanocomposites. Part I: structural characterization and quantifying clay dispersion by melt rheology. Polymer 48, 4492-4502.
Fornes, T.D., Yoon, P.J., Keskkula, H., Paul, D.R., 2001. Nylon 6 nanocomposites: the effect of matrix molecular weight. Polymer 42, 9929-9940.
Fornes, T.D., Yoon, P.J., Paul, D.R., 2003. Polymer matrix degradation and color formation in melt processed nylon 6/clay nanocomposites. Polymer 44, 7545-7556.
Galuska, A.A., 1997. Quantitative surface analysis of ethylene-propylene polymers using Tof-SIMS. Surf. Interface Anal. 25, 1-4.
IJdo, W.L., Kemnetz, S., Benderly, D., 2006. An Infrared method to assess organoclay delamination and orientation in organoclay polymer nanocomposites. Polym. Eng. Sci. 46, 1031-1039.
Kim, S.W., Jo, W.H., Lee, M.S., Ko, M.B., Jho, J.Y., 2002. Effects of shear on melt exfoliation of clay in preparation of Nylon 6/Organoclay nanocomposites. Polym. J. 34, 103-111.
Lertwimolnun, W., Vergnes, B., 2006. Effect of processing conditions on the formation of polypropylene/organoclay nanocomposites in a twin-screw extruder. Polym. Eng. Sci. 46, 314-323.

Lertwimolnun, W., Vergnes, B., 2007. Influence of screw profile and extrusion conditions on the microstructure of polypropylene/organoclay nanocomposites. Polym. Eng. Sci. 47, 2100-2109.
Médéric, P., Ville, J., Huitric, J., Moan, M., Aubry, T., 2011. Effect of processing procedures and conditions on structural, morphological and rheological properties of Polyethylene/Polyamide/Nanoclay blends. Polym. Eng. Sci. 51, 969-978.
Modesti, M., Lorenzetti, A., Bon, D., Besco, S., 2005. Effect of processing conditions on morphology and mechanical properties of compatibilized polypropylene nanocomposites. Polymer 46, 10237-10245.
Mould, S., Barbas, J.M., Machado, A.V., Nóbrega, J.M., Covas, J.A., 2011. Measuring the rheological properties of polymer melts with on-line rotational rheometry. Polym. Test. 30, 602-610.
Nassar, N., Utracki, L.A., Kamal, M.R., 2005. Melt intercalation in montmorillonite/ polystyrene nanocomposites. Int. Polym. Process. 20, 423-431.
Pavlidou, S., Papaspyrides, C.D., 2008. A review on polymer-layered silicate nanocomposites. Prog. Polym. Sci. 33, 1119-1198.
Shah, R.K., Paul, D.R., 2006. Organoclay degradation in melt processed polyethylene nanocomposites. Polymer 47, 4075-4084.
Spencer, M.W., Cui, L., Yoo, Y., Paul, D.R., 2010. Morphology and properties of nanocomposites based on HDPE/HDPE-g-MA blends. Polymer 51, 1056-1070.
Tanoue, S., Utracki, L.A., Garcia-Rejon, A., Ttibouet, J., Cole, K.C., Kamal, M.R., 2004. Melt compounding of different grades of polystyrene with organoclay. Part 1: compounding and characterization. Polym. Eng. Sci. 44, 1046-1060.

Treece, M.A., Zhang, W., Moffit, R.D., Oberhauser, J.P., 2007. Twin-screw extrusion of polypropylene-clay nanocomposites: Influence of masterbatch processing, screw rotation mode and sequence. Polym. Eng. Sci. 47, 898-911.
Vaia, R.A., Ishii, H., Giannelis, E.P., 1993. Synthesis and properties of twodimensional nanostructures by direct intercalation of polymer melt in layered silicates. Chem. Mater. 5, 1694-1696.
Vergnes, B., 2011. The use of apparent yield stress to characterize exfoliation in polymer nanocomposites. Int. Polym. Process. 26, 229-232.

Vermogen, A., Masenelli-Varlot, K., Séguéla, R., Duchet-Rumeau, J., Boucard, S., Prele, P., 2005. Evaluation of the structure and dispersion in polymer-layered silicate nanocomposites. Macromolecules 38, 9661-9669.
Xie, W., Gao, Z., Pan, W.-P., Hunter, D.L., Singh, A., Vaia, R., 2001. Thermal degradation chemistry of alkyl quaternary ammonium montmorillonite. Chem. Mater. 13, 2979-2990.
Xu, L., Nakajima, H., Manias, E., Krishnamoorti, R., 2009. Tailored nanocomposites of polypropylene with layered silicates. Macromolecules 42, 3795-3803.
Yan, L., Roth, C.B., Low, P.F., 1996. Changes in the Si-O vibrations of smectite layers accompanying the sorption of interlayer water. Langmuir 12, 4421-4429.
Zouari, R., Domenech, T., Vergnes, B., Peuvrel-Disdier, E., 2012. Time evolution of the structure of organoclay/polypropylene nanocomposites and application of the time-temperature superposition principle. J. Rheol. 56, 725-742.